International Journal of Fluid Machinery and Systems
Vol. 2, No. 3, July-September 2009

Original Paper

Cause of Cavitation Instabilities in Three Dimensional Inducer

Donghyuk Kang[1], Koichi Yonezawa[1], Hironori Horiguchi[1], Yutaka Kawata[2] and Yoshinobu Tsujimoto[1]

[1]Graduate School of Engineering Science, Osaka University
1-3 Machikaneyama, 560-8531, Toyonaka, Osaka, Japan
[2]Department of Mechanical Engineering, Osaka Institute of Technology
5-16-1, Omiya, Asahi-Ku, 535-8505, Osaka, Japan

Abstract

Alternate blade cavitation, rotating cavitation and cavitation surge in rocket turbopump inducers were simulated by a three dimensional commercial CFD code. In order to clarify the cause of cavitation instabilities, the velocity disturbance caused by cavitation was obtained by subtracting the velocity vector under non-cavitating condition from that under cavitating condition. It was found that there exists a disturbance flow towards the trailing edge of the tip cavity. This flow has an axial flow component towards downstream which reduces the incidence angle to the next blade. It was found that all of the cavitation instabilities start to occur when this flow starts to interact with the leading edge of the next blade. The existence of the disturbance flow was validated by experiments.

Keywords: Inducer, Cavitation instabilities, Velocity disturbance, Three dimensional CFD

1. Introduction

In modern turbopumps for rocket engines, it is generally recognized that cavitation instabilities are major concerns [1]. They occur in the range where the head is not yet decreased, and cause the high dynamic loads on the shaft and the blades.

By a two dimensional stability analysis for blade surface cavity in cascades [2], it was found that the steady cavity length is the dominating factor of cavitation instabilities and that various modes of cavitation instability start to occur when the cavity length becomes about 65% of blade circumferential spacing. This result agrees reasonably with experiments for three dimensional inducers if we consider the cavity length at the tip. By the two dimensional stability analysis for alternate blade cavitation [3], it was shown that alternate blade cavitation also starts to occur when the cavity length becomes about 65% of the blade circumferential spacing. By a closer observation of the flow field around alternate blade cavitation, it was found that there exists a region near the cavity trailing edge where the velocity vector is tilted towards the suction surface. When this region gets closer to the leading edge of the next blade, the incidence angle to the next blade gets smaller and the cavity length on the next blade becomes smaller, hence it results in alternate blade cavitation. However, the flow field was obtained with a closed cavity model of blade surface cavitation and the explanation cannot be directly applied to tip cavities in real 3D inducers.

Hosangadi, A., et al[4] successfully simulated rotating cavitation in a cavitating inducer by an unsteady three dimensional simulation and discussed the cause of cavitation instabilities. They observed rotational cavitation modes and explained that the interaction of the cavity with the next blade leads to cavitation instabilities. The cavity forming on the pressure side of the blade leads to the reversal in the blade loading, altering the incidence angle to the next blade, and hence it results in the rotational cavitation modes.

The present paper focuses on the clarification of the mechanism of cavitation instabilities in real three dimensional flow based on detailed analyses of the velocity field under cavitation instabilities obtained by using a commercial three dimensional CFD code.

2. Specification of Inducers

Figure 1 and Table 1 show the main dimensions of 4 and 3-bladed inducers with the backward leading edge sweep and the diameter of 149.8mm. The inlet and outlet blade angles are 7.5 deg. and 9.0 deg. at the tip, respectively. The design flow coefficient ϕ_d is 0.078. The flow coefficient ϕ is defined as v_1/U_t, where v_1 is the mean axial velocity in the plane at $z/D_t=0$, and U_t is the tip speed of the impeller. The axial coordinate z is set in the downstream direction from the origin at the leading edge of blades at root as shown in Fig. 1(b).

Received June 24 2009; accepted for publication July 7 2009: Review conducted by Prof. Youn-Jea Kim. (Paper number O09021)
Corresponding author: Mr. Donghyuk Kang, kang@me.es.osaka-u.ac.jp

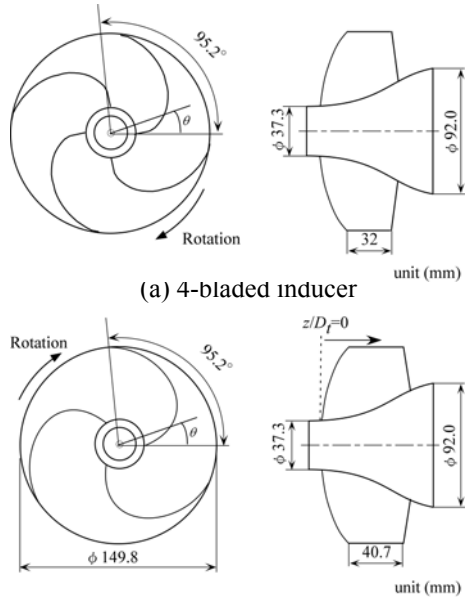

Fig. 1 Leading edge geometry for the 3 and 4-bladed inducers

Table 1 Geometrical properties for the 3 and 4-bladed inducers

Number of blades	3-bladed inducer	4-bladed inducer
Tip diameter	149.8 mm	←
Inlet tip blade angle	7.5 deg	←
Outlet tip blade angle	9.0 deg	←
Hub/tip ratio at the inlet	0.25	←
Hub/tip ratio at the outlet	0.51	0.53
Solidity at tip	1.91	←
Design flow coefficient	0.078	←
Tip clearance	0.5 mm	←
Blade thickness at tip	2 mm	←

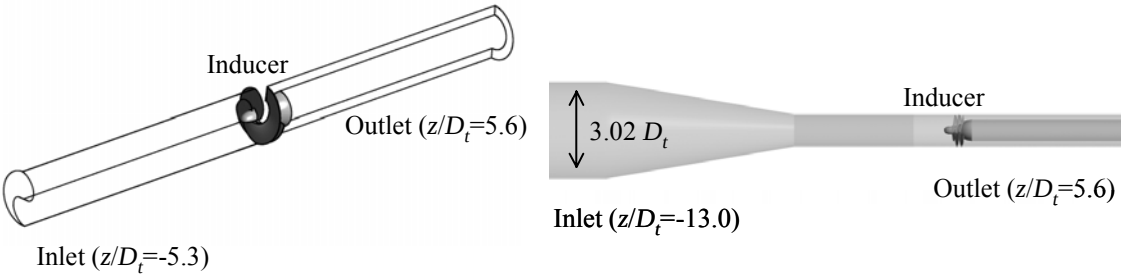

Fig. 2 Computational domain

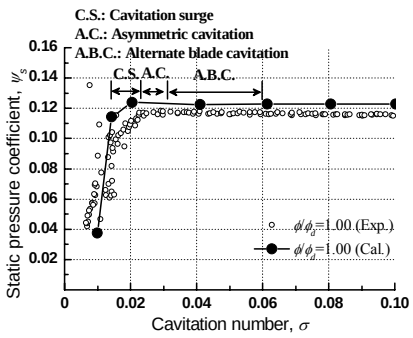

Fig. 3 Suction performance curve with the occurrence regions of the cavitation instabilities for the 4-bladed inducer

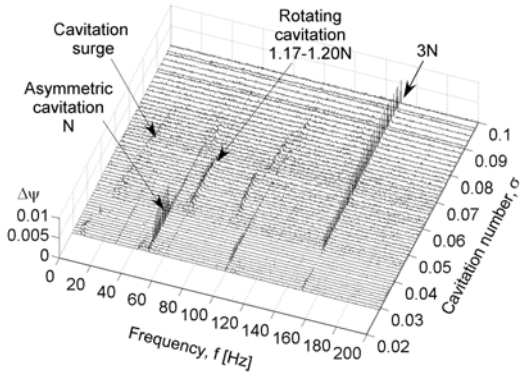

Fig. 4 Spectrum of inlet pressure fluctuations measured at the inlet of 3-bladed inducer, at ϕ/ϕ_d=1.0 and 3000rpm

3. Computation Method

A commercial software, ANSYS-CFX11.0, was used for the simulation of cavitating flows in inducers. The simplified Reyleigh-Plesset model was applied as the cavitation model. The k-ω turbulence model was used. Zero circumferential velocity and the total pressure were specified at the inlet and constant mass flow rate was specified at the outlet. The working fluids were water and its vapor. The rotational speed was fixed at 3000rpm which is the same as experiments. For the simulation of alternate blade cavitation, steady flow calculations in two blade channels of the 4-bladed inducer were made by assuming the periodicity over 2 blades, as shown in Fig. 2(a). The number of computational cells is about 2,200,000. For the simulation of rotating cavitation and cavitation surge, unsteady flow calculations were made for all blades of the 3-bladed inducer. The time step was

Table 2 Cavitation instabilities and their frequencies for various cavitation numbers, by computations at ϕ/ϕ_d=1.0

Cavitation number	Instability name	Frequency
σ=0.10	Steady cavitation	-
σ=0.050	Cavitation surge	0.33N
σ=0.045	Cavitation surge	0.31N
σ=0.040	Rotating cavitation	1.20N
σ=0.035	Rotating cavitation → Cavitation surge	1.2N → 0.22N
σ=0.030	Asymmetric cavitation → Cavitation surge → Divergence	-

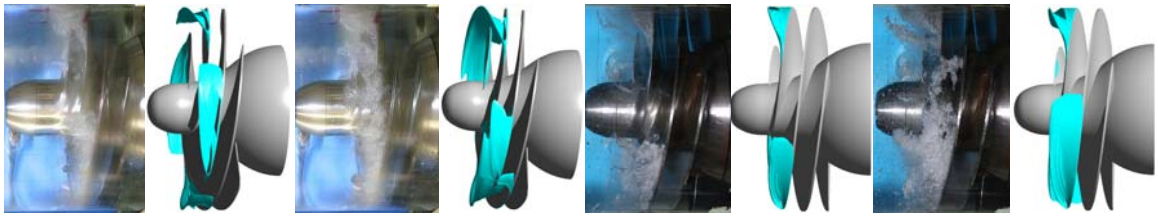

(a) σ= 0.06 (b) σ = 0.04 (c) σ = 0.02 (d) σ = 0.01

Fig. 5 Cavity shape for the 4-bladed inducer at ϕ=0.078, 3000rpm

(a) σ = 0.1 (b) σ = 0.06 (c) σ = 0.04 (d) σ = 0.03 (Exp.), 0.02 (Cal.)

Fig. 6 The same as the Fig.5, for the 3-bladed inducer at ϕ=0.078, 3000rpm

1/400 of a revolution of the impeller. The second order schemes in space and time were used. To obtain stable solution, the inlet pipe was enlarged as shown in Fig. 2(b). The number of computational cells is 3,300,000.

4. Comparison with Experiments

Figures 3 shows the regions of various cavitation instabilities observed in experiments with the suction performance curve at ϕ/ϕ_d =1.0, for the 4-bladed inducer. The horizontal axis shows the cavitation number defined as $(p_1\text{-}p_v)/(\rho U_t^2/2)$ where p1 is the inlet pressure measured 302mm upstream of the blade leading edge at the tip and pv is the vapor pressure. The vertical axis shows the static pressure coefficient s defined as $(p_2\text{-}p_1)/(\rho U_t^2)$, where the p2 is the outlet pressure measured 66mm downstream of the blade leading edge at the tip. In experiments, the cavitation instability was identified by the inlet pressure fluctuations measured by pressure transducers flush mounted 44mm upstream of the blade leading edge at the tip. The inlet pressure and flow rate were adjusted by the vacuum pump and the flow control valve, respectively. The real flow rates at lower cavitation numbers are somewhat different with the nominal flow rate set at higher cavitation number. If the real flow rate and cavitation number were exactly controlled, cavitation instabilities always occur at the same conditions. The suction performance curve at ϕ/ϕ_d =1.0 is evaluated by the steady CFD computations is also shown. Alternate blade cavitation occurred in 0.03<σ<0.06 in experiments and at σ=0.04 and 0.02 in steady CFD computations.

Figure 4 shows the spectrum of pressure fluctuations measured at the inlet of the 3-bladed inducer, at ϕ/ϕ_d =1.0 and 3000rpm. We observe rotating cavitation for 0.047<σ<0.064 and asymmetric cavitation for 0.033<σ<0.047. Although weak, we observe cavitation surge in a wide range of σ. In unsteady CFD computations at ϕ/ϕ_d=1.0 various cavitation instabilities were observed as shown in Table 2. The frequencies were obtained by the pressure oscillation measured 44 upstream of the blade leading edge, which is the same as experiments. Cavitation surges were found at σ=0.05,0.045 and 0.035. The frequency of cavitation surge decreases as the cavitation number is decreased, in reasonable agreement with experiments. Rotating cavitation was observed at σ =0.040 and its frequency is in reasonable agreement with experiments. At σ=0.030, asymmetric cavitation was observed at an early stage but it switched to cavitation surge and eventually diverged. Although the value of σ for each instability is different from the experiment, the order of their appearance with reducing σ agrees with the experiment.

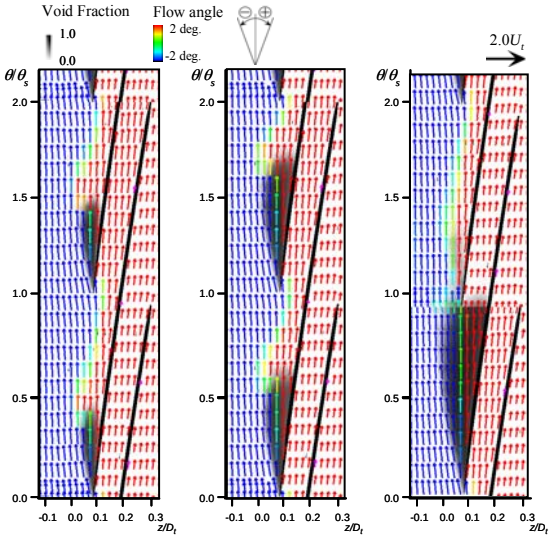

(a) σ=0.10 (b) σ=0.06 (c) σ=0.04

Fig. 7 Relative velocity vector and void fraction and flow angle distributions in z-θ plane at r/R_t=0.98, ϕ=0.078, 3000rpm

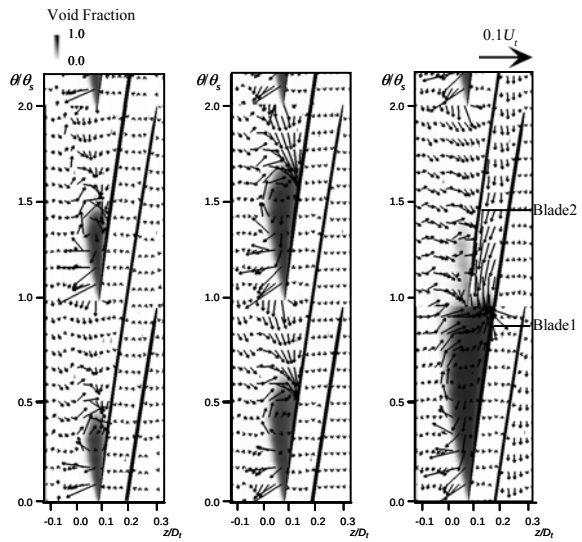

(a) σ=0.10 (b) σ=0.06 (c) σ=0.04

Fig. 8 Disturbance velocity vector and void fraction distribution in z-θ plane at r/R_t=0.98, ϕ=0.078, 3000rpm

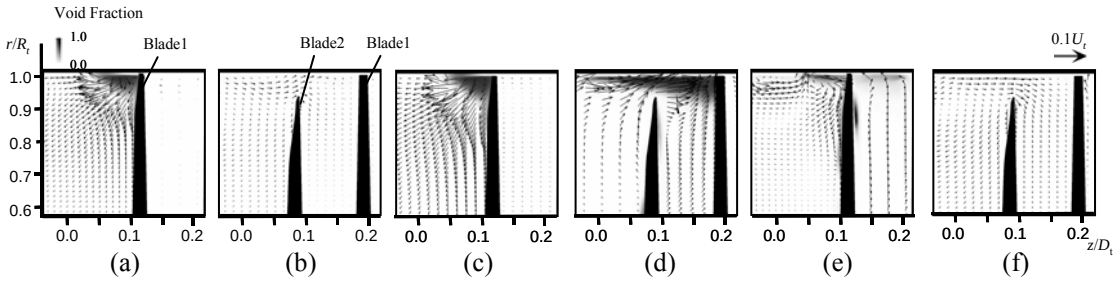

Fig. 9 Disturbance velocity vector and void fraction distribution in meridional plane at ϕ=0.078, 3000rpm
σ=0.06: (a) θ/θ_s=0.2, (b) θ/θ_s=0.9 σ=0.04: (c) θ/θ_s=0.2, (d) θ/θ_s=0.9, (e) θ/θ_s=1.2, (f) θ/θ_s=1.9

Figures 5 and 6 show the cavity shape for the 4 and 3-bladed inducers, respectively, obtained from experiments and steady CFD computations. The cavity was shown by a plane with the void fraction α=0.01. When the cavity length becomes about 65% of the blade circumferential spacing, alternate blade cavitation occurs as shown in Fig.5(b), in agreement with the two dimensional stability analysis. In the experiment for the 3-bladed inducer, rotating cavitation starts at σ=0.064 when the cavity length becomes about 65% of the blade circumferential spacing as shown in Fig. 6(b) (Average cavity is shown). The steady CFD code can simulate the tip cavity shape reasonably except for backflow vortex cavitation.

5. Alternate Blade Cavitation

Since the cavities on each blade are steady for alternate blade cavitation, the steady CFD can simulate alternate blade cavitation in the 4-bladed inducer. Figure 7 shows the relative velocity vector, void fraction and flow angle distributions in the axial-circumferential plane at r/Rt=0.98. Unlike blade surface cavitation, the velocity vector obtained by the bubbly flow model is not parallel with the cavity surface. The flow angle is negative in the upstream due to the backflow. We can observe a region with the positive flow angle downstream of the cavity trailing edge. To clarify the effect of cavitation, the disturbance velocity vector was evaluated by subtracting the velocity of non-cavitating flow from that of cavitating flow, and shown in Fig.8. We can observe a source-like flow around the cavity leading edge and a flow towards the cavity trailing edge. These flows are caused by the growth and collapse of cavitation bubbles. The velocity vector towards the cavity trailing edge has an axial flow component toward downstream. When the local flow near the cavity trailing edge starts to interact with the leading edge of the next blade, as shown in Fig. 8(b), the incidence angle to the next blade is reduced and the cavity size on the next blade is decreased. This results in alternate blade cavitation shown in Fig. 8(c).

Figure 9 shows the disturbance velocity vector and the void fraction distribution in meridional planes at θ/θ_s=0.2 and 0.9. The source-like flow near the cavity leading edge are shown in Figs. 9 (a) and (c). The flow towards the trailing edge of the longer cavity of alternate blade cavitation is shown in Fig. 9(d). This figure clearly shows how the incidence angle to the next blade at z/D_t=0.09 is decreased. The radial component of the velocity disturbance is much smaller than the axial component. This is why the interaction of local flow near the cavity trailing edge with the leading edge of the next blade is important for tip cavities.

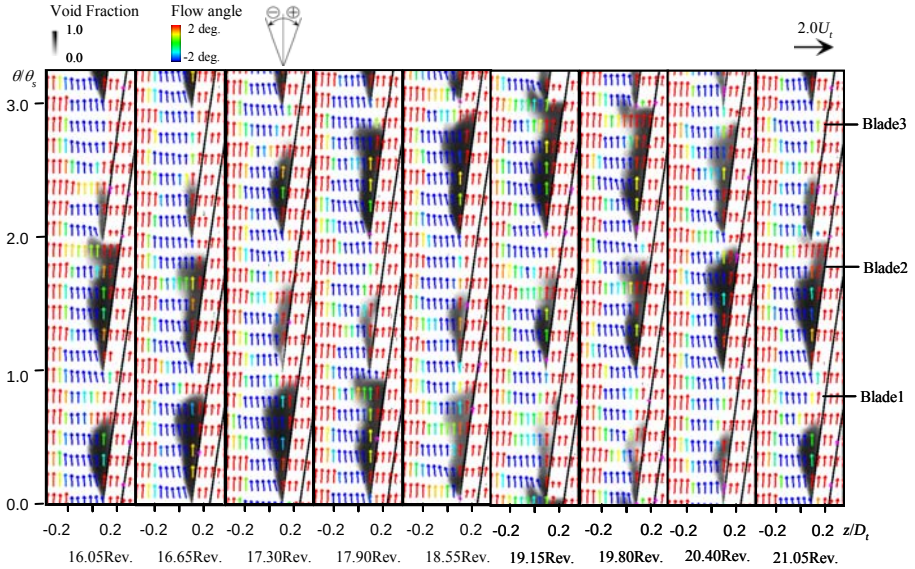

Fig. 10 Relative velocity vector, void fraction and flow angle distributions in z-θ plane at r/R_t=0.98, ϕ=0.078, σ=0.04, 3000rpm

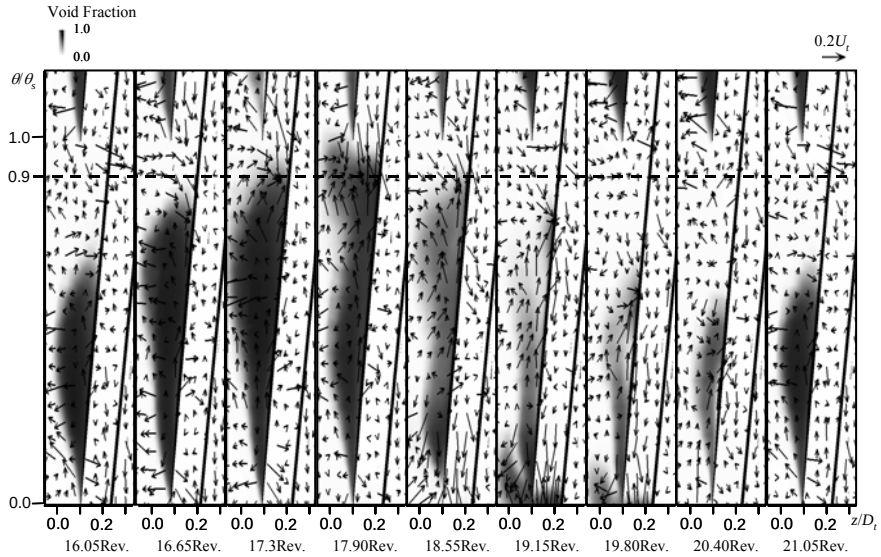

Fig. 11 Disturbance velocity vector and void fraction distribution in z-θ plane at r/R_t=0.98, ϕ=0.078, σ=0.04, 3000rpm

6. Rotating Cavitation

In order to simulate rotating cavitation, we carried out unsteady cavitating flow of 3-bladed inducer at ϕ/ϕ_d =1.0, σ =0.04. In experiments, rotating cavitation was observed in 0.047<σ< 0.065 at ϕ/ϕ_d =1.0. Figure 10 shows the relative velocity vector, void fraction and flow angle distributions in the axial-circumferential plane at r/R_t=0.98. The propagation speed of rotating cavitation is about 1.2 times rotating speed of impeller. This propagation speed is reasonable as compared with experiments. We can explain the propagation of the cavity as follows. We focus on the growth of the cavity on each blade during 16.05Rev.~17.9Rev. shown in Fig.10. If the cavity on blade 1 gets larger, the incidence angle to blade 2 is decreased and the cavity length on the blade is decreased. Due to the decrease of the cavity length on blade 2, the incidence angle to blade 3 is increased and the cavity on blade 3 grows.

Figure 11 shows the disturbance velocity vector in axial-circumferential plane at r/R_t=0.98. Due to the oscillation of the cavity itself, the disturbance velocity field is not as clear as for alternate blade cavitation shown in Fig.8. However, we can observe a source-like flow near the cavity leading edge and the flow towards the cavity trailing edge.

Figure 12 shows the disturbance velocity vector and the void fraction distribution in meridional plane at θ/θ_s=0.9. We can observe that the flow near the leading edge of blade 2 is subjected to higher axial disturbance velocity at the cavity trailing edge on blade 1. Thus, the propagation of rotating cavitation can be explained by the interaction of the flow towards the cavity trailing edge with the next blade.

Figure 13 shows the pressure distribution in z-θ plane at r/R_t=0.98. The local cavitation number σ_c is defined as $(p-p_v)/(0.5\rho U_t^2)$. We observe a high pressure region near the cavity trailing edge as typically shown on blade 1 at 16.05Rev.. This is caused by the flow stagnation near the cavity trailing edge. When the cavity length becomes larger, the high pressure region extends to the suction surface of the next blade leading edge. Then, the cavity length on the next blade gets shorter. Thus, the propagation can be also explained from the pressure distribution.

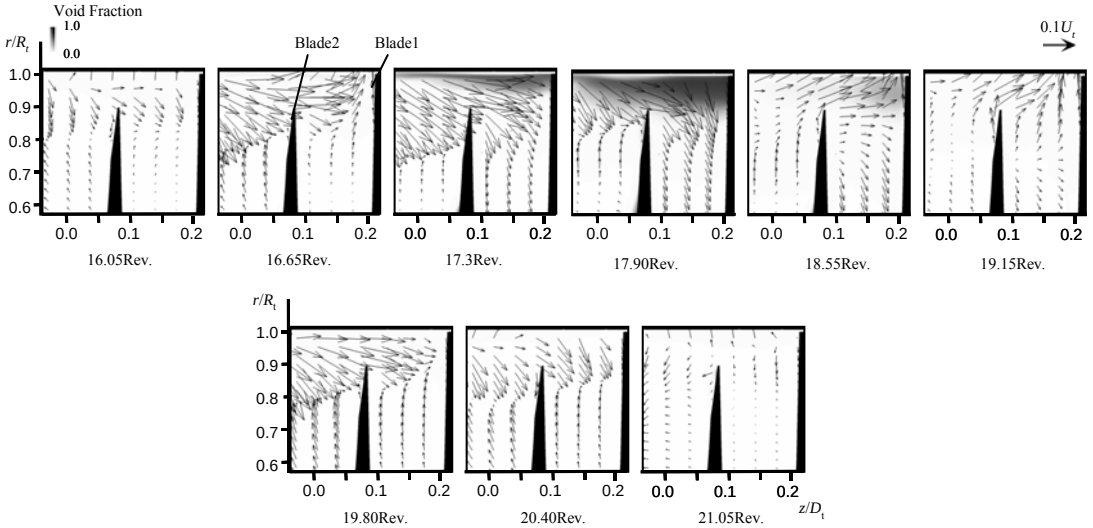

Fig. 12 Disturbance velocity vector and void fraction distribution in meridional plane at θ/θ_s=0.9, ϕ=0.078, σ=0.04, 3000rpm

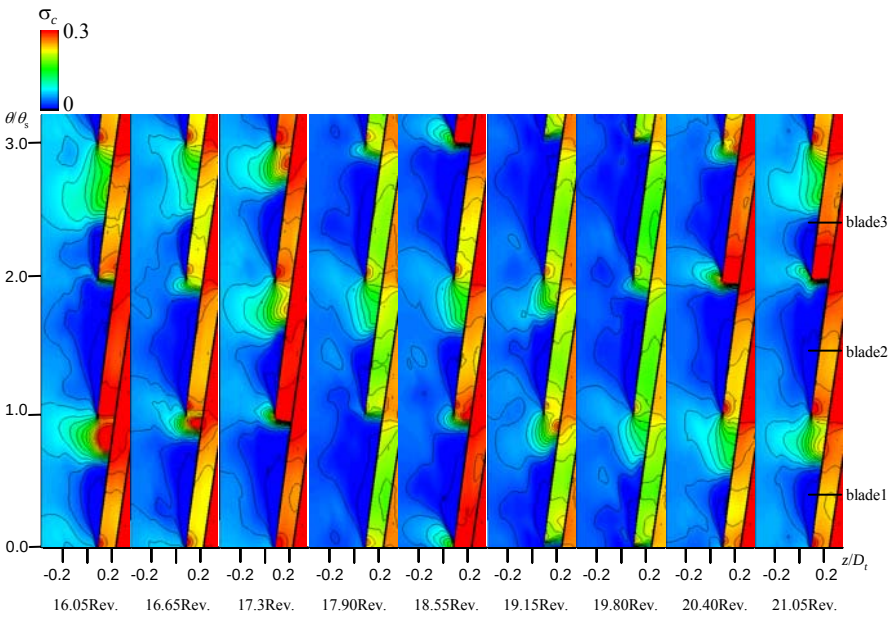

Fig. 13 Unsteady pressure distribution under rotating cavitation at r/R_t=0.98, ϕ=0.078, σ=0.04, 3000rpm

7. Cavitation Surge

Figure 14 shows the relative velocity vector, void fraction and flow angle distributions in the axial-circumferential plane at r/R_t=0.98, ϕ/ϕ_d =1.0 and σ =0.035. The flow data at ϕ/ϕ_d =1.0 and σ =0.04 under rotating cavitation was used the initial value for the calculation of cavitating surge at ϕ/ϕ_d =1.0 and σ =0.035. We observe a rotating cavitation in 6.0~11.0Rev., but it switched to cavitation surge at 11.6Rev. The frequency of cavitation surge is about 0.2N, where N is the frequency 50Hz of the impeller rotation. This frequency is reasonable as compared with experiments. In the experiment, cavitation surge was observed in a wide range of $0.03<\sigma<0.08$ at ϕ/ϕ_d =1.0 as shown in Fig.4.

Figure 15 shows the disturbance velocity vector around blade 1. When the cavity is shed from the trailing edge, the flow toward the shed cavity is more evident.

Figure 16 shows the disturbance velocity vector in meridional planes at θ/θ_s=0.9,1.9 and 2.9. The disturbance velocity is small for all blades when the cavity is small (17.3Rev.) and we observe a strong axial velocity disturbance for all blades when the cavity is large (19.2Rev.). Thus cavitation surge also can be explained from the interaction of the disturbance flow near the cavity trailing edge with the next blade.

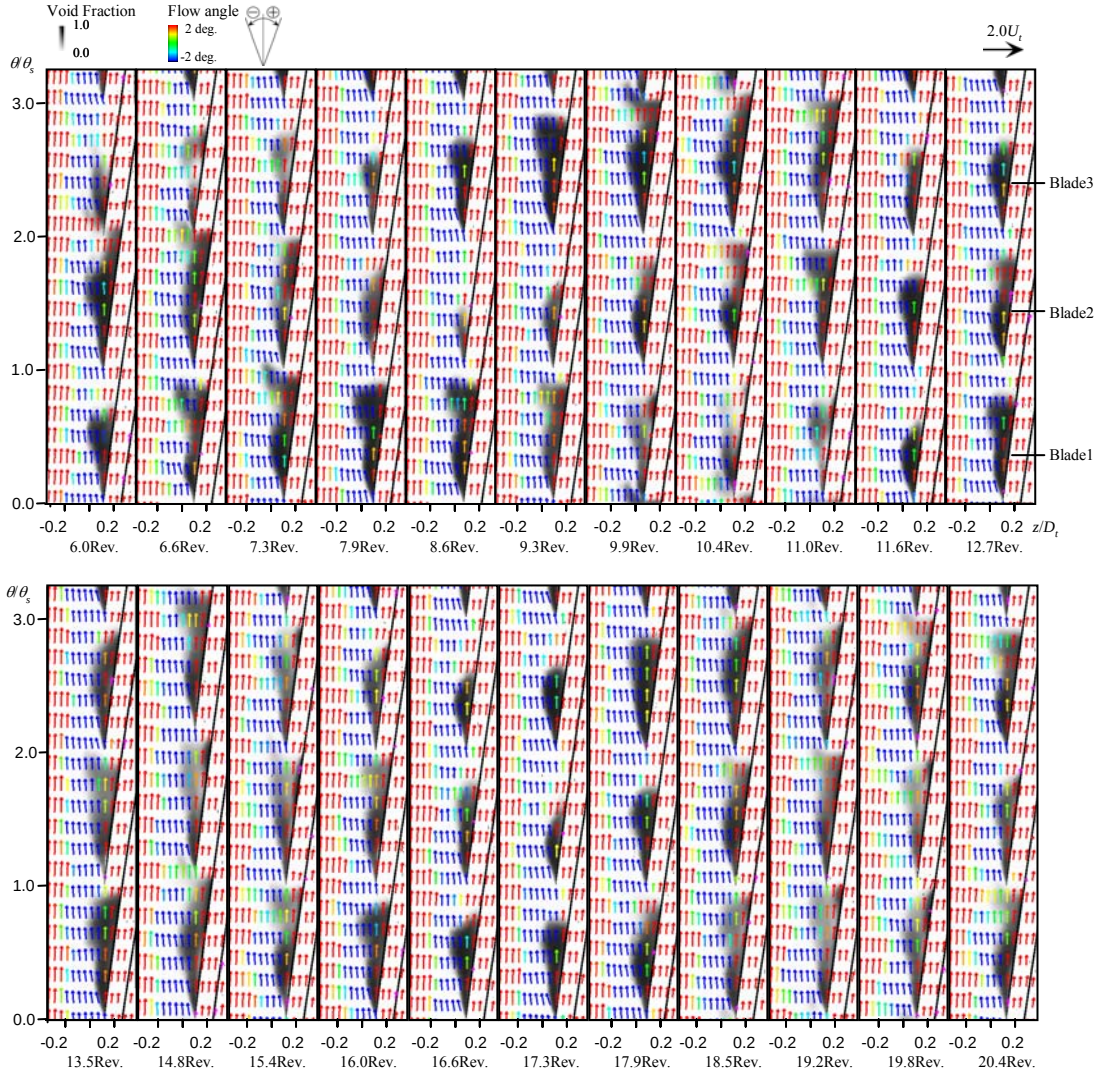

Fig. 14 Relative velocity vector, void fraction and flow angle distributions in z-θ plane at r/R_t=0.98, ϕ=0.078, σ=0.035, 3000rpm

8. Disturbance Velocity Measurements

Since it has been shown that the disturbance velocity due to tip cavity plays an important role in cavitation instabilities, velocity measurements were made with the 4-bladed inducer. The absolute velocity was measured by using LDV (Kanomax, probe:FLVP-K(Model 1884), laser unit:FLV8851, signal processing board 8008). About 10~40 data were averaged at each measurement point. The cavity shape was evaluated from pictures. The velocity measurement were made at σ=0.375 and σ=0.10 and relative velocity near the leading edge is shown in Fig.17(a) and (b). Since the cavity is small at σ=0.375, the velocity disturbance due to cavity is evaluated by subtracting the velocity vector at σ=0.375 from that at σ=0.10 and shown in Fig.17(c). Although the scatter is large, we can observe a source-like flow near the cavity leading edge and the flow towards the cavity trailing edge. This result is similar to the disturbance vectors shown in Fig.8(a) and validates the results of numerical simulation.

9. Conclusion

It was found that there exists a disturbance flow toward the trailing edge of tip cavity. The existence of this disturbance flow was confirmed by experiments. This flow has an axial flow component towards downstream which reduces the incidence angle to the next blade. It was found that all of the cavitation instabilities start to occur when this flow starts to interact with the leading edge of the next blade. This explains why various cavitation instabilities occur, when the tip cavity length becomes about 65% of the blade circumferential spacing. This also suggests that cavitation instabilities can be avoided by avoiding the interaction of the tip cavity with the next blade. Actually several stable inducers could be designed based on this design guideline [5].

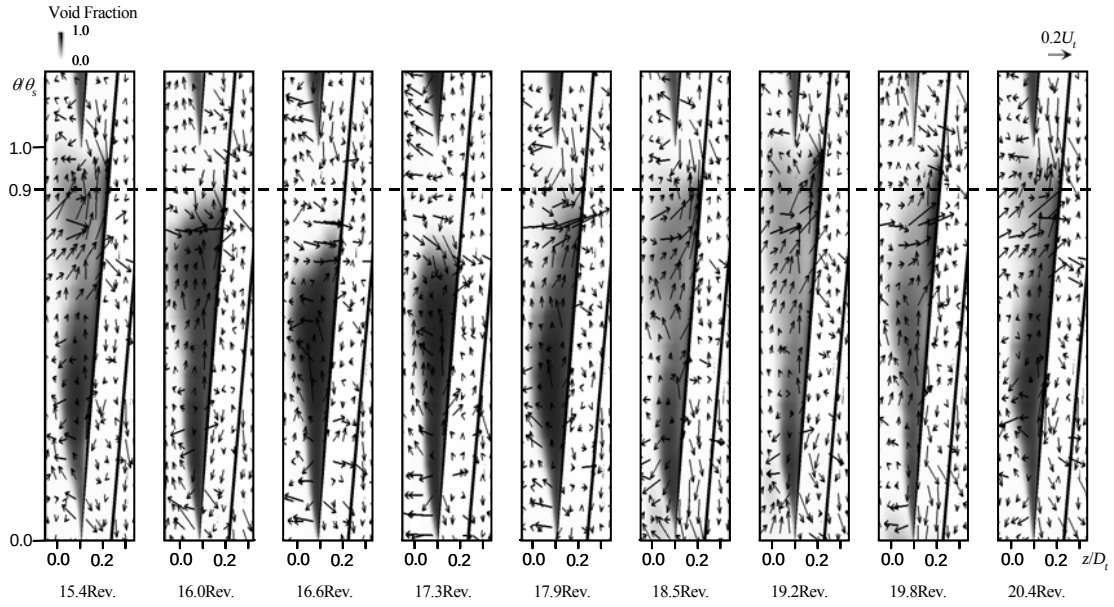

Fig. 15 Disturbance velocity vector and void fraction distribution in z-θ plane at r/R_t=0.98, ϕ=0.078, σ=0.035, 3000rpm

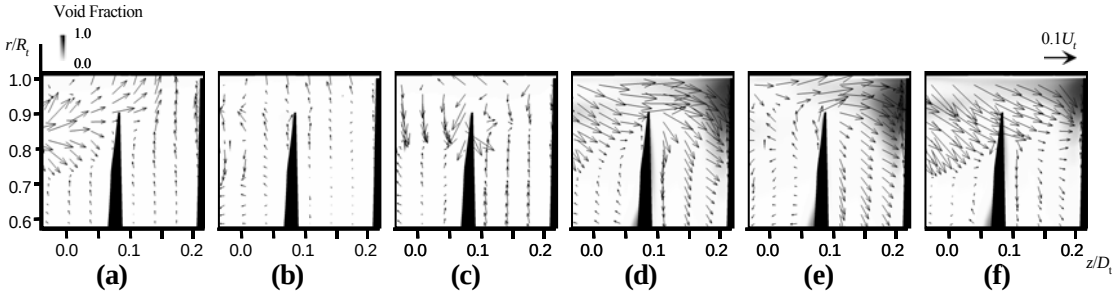

Fig. 16 Disturbance velocity vector and void fraction distribution in meridional plane at σ=0.035 ,ϕ=0.078, 3000rpm
17.3Rev.: (a) θ/θ_s=0.9, (b) θ/θ_s=1.9, (c) θ/θ_s=2.9
19.2Rev.: (d) θ/θ_s=0.9, (e) θ/θ_s=1.9, (f) θ/θ_s=2.9

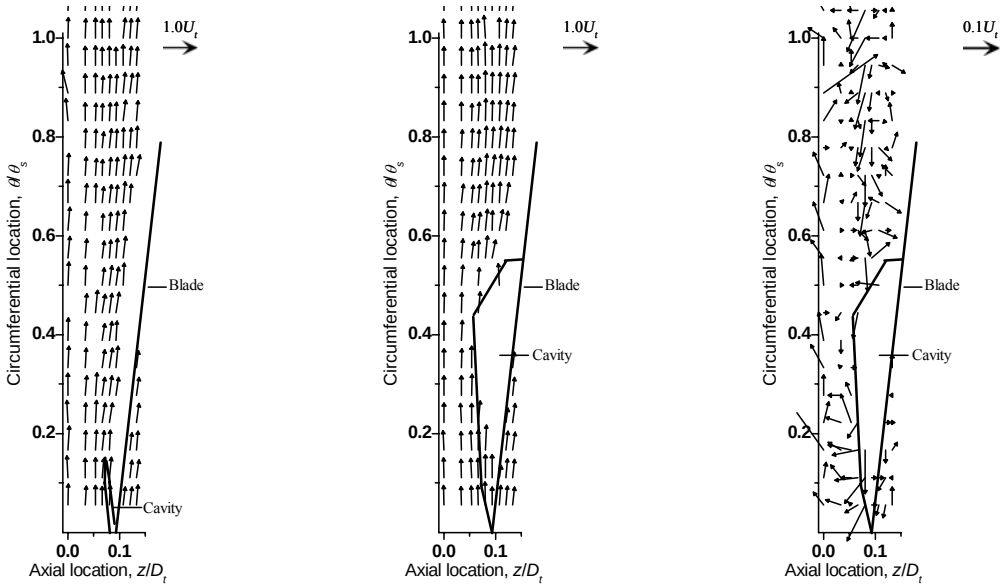

(a) Relative velocity vector, σ=0.375

(b) Relative velocity vector, σ=0.10

(c) Disturbance velocity vector

Fig. 17 Velocity vectors obtained from experiments at r/R_t=0.98, ϕ=0.078, 3000rpm

Acknowledgments

The experiment was carried out with the help of Arimoto Yusuke and Aono Jun. Authors would like to thank their contributions. This research was performed funded by Grant-in-Aid for Scientific Research of Japan Society for the Promotion of Science.

Nomenclature

D_t	Diameter of inducer [m]	α	Void Fraction
f	Frequency of pressure fluctuation [Hz]	β_t	Blade angle at the tip [degree]
N	Frequency of impeller rotating [Hz]	β_1, β_2	Inlet and outlet blade angles at the tip [degree]
p_1	Pressure at the inlet [Pa]	ϕ	Flow coefficient = v_1/U_t
p_2	Pressure at the outlet [Pa]	ϕ_d	Design flow coefficient =0.078
p_v	Vapor pressure [Pa]	θ	Circumferential location [m]
r	Radial location [m]	θ_s	Circumferential spacing [m]
R_t	Radius of inducer [m]	ρ	Density of water [kg/m^3]
U_t	Tip speed [m/s]	σ	Cavitation number =$(p_1-p_v)/(\rho U_t^2/2)$
v_1	Mean axial velocity at the inlet (z/D_t=0) [m/s]	σ_c	Local cavitation number =$(p-p_v)/(\rho U_t^2/2)$
z	Axial location measured from the root of the leading edge [m]	ψ_s	Pressure coefficient =$(p_2-p_1)/(\rho U_t^2)$
		$\Delta\psi$	Fluctuating pressure coefficient =$\Delta p/(\rho U_t^2)$

References

[1] Tsujimoto, Y., Horiguchi, H., Fujii, A., 2004, “Non-Standard Cavitation Instabilities in Inducers,” Proceedings of the 10th International Symposium on Transport Phenomenon and Dynamic of Rotating Machinery, ISROMAC10-2004-020, pp. 1-11.

[2] Horiguchi,H.,Watanabe,S.,Tsujimoto,Y., 2000, “A Linear Stability Analysis of Cavitation in a Finite Blade Count impeller,” ASME Journal of Fluids Engineering, Vol. 122, pp. 798-805

[3] Horiguchi,H.,Watanabe,S.,Tsujimoto,Y. and Aoki, M., 2000, “Theoretical Analysis of Alternate Blade Cavitation in Inducers,” ASME Journal of Fluids Engineering, Vol. 122, No. 1, pp. 156-163.

[4] Hosangadi, A., Ahuja, V., Ungewitter, R.J., “Simulation of Rotational Cavitation Instabilities in the SSME LPFP Inducer,” AIAA-2007-5536.

[5] Kang, D., Watanabe, T., Yonezawa, K., Horiguchi, H., Kawata, Y., Tsujimoto, Y., 2009, “Inducer Design to Avoid Cavitation Instabilities,” Proceeding of the 61st Turbo Machinery of Japan Conference, pp. 33-38, (in Japanese).